



Removal of metronidazole antibiotic pharmaceutical from aqueous solution using TiO₂/Fe₂O₃/GO photocatalyst: Experimental study on the effects of mineral salts

Negin Entezami, Mehrdad Farhadian*, Nila Davari

Department of Chemical Engineering, Faculty of Engineering, University of Isfahan, Isfahan, Iran

ARTICLE INFO

Article history:

Received 7 December 2019

Received in revised form

25 March 2020

Accepted 2 April 2020

Keywords:

Mineral salts

Reaction rate constant

Titanium dioxide

Graphene oxide

Iron oxide (III)

ABSTRACT

A TiO₂/Fe₂O₃/GO photocatalyst is synthesized via the sol-gel method and characterized by X-Ray Diffraction (XRD), X-Ray Fluorescence (XRF), FT-IR, Brunauer-Emmett-Teller (BET), and Ultraviolet-Visible Diffuse Reflection Spectroscopy (UV-Vis DRS) analyses. Metronidazole (MET) concentration (10-20 mg/L), photocatalyst concentration (0.5-1.5 g/L), irradiation time (60-120 min), and initial pH (4-6) are investigated through response surface methodology (RSM), and the optimal process conditions are determined. The removal efficiency of MET with the TiO₂/Fe₂O₃/GO photocatalyst is 97% under optimal conditions: a pollutant concentration of 10 mg/L, the irradiation time of 120 min, photocatalyst concentration of 1 g/L, and pH of 5. The influence of mineral salts concentrations (50-800 mg/L), including NaCl, Na₂SO₄, NaHCO₃, KCl, MgSO₄, and CaCl₂, are examined at the initial pH of 5, photocatalyst concentration of 1 g/L, and pollutant concentration of 20 mg/L. According to the results, the reaction rate constant decreases with an increase in mineral salts concentrations up to 800 mg/L, especially with Na₂SO₄ (42.43% deactivation) and also with MgSO₄ (38.08%) and NaHCO₃ (37.73%), under the same operational conditions. The effects of mineral salts such as NaCl and KCl on the reaction rate constant for the contaminant removal efficiency have a downward trend until these salts reach a 200 mg/L concentration, and then they experience an upward trend.

1. Introduction

Antibiotics have been frequently detected in the environment in recent decades, leading to severe environmental pollution and human health hazards [1-3]. One of the most widely used antibiotics in the world is metronidazole, which is used to treat infectious diseases caused by anaerobic bacteria and protozoa [4]. MET is also employed to remove parasites in cattle, poultry, and fish feed [5]. MET is not efficiently eliminated by conventional treatment methods because it is stable, non-biodegradable, and highly soluble [6]. The accumulation of MET in aquatic environments has detrimental effects on living creatures considering its toxicity, carcinogenicity, mutagenicity, and

increasing antimicrobial resistance [7]. As a result, the removal of MET from contaminated water resources is vital to protect the environment [8]. Its removal from polluted water has been performed by advanced oxidation processes (AOPs), including heterogeneous photocatalysis, UV/H₂O₂, photolysis, ozonation, Fenton, photo-Fenton, electro-Fenton, heterogeneous Fenton-like, electrocatalysis, and O₃/H₂O₂ [9-12]. Pharmaceutical compounds are oxidized and converted to H₂O, CO₂, and inorganic acids by hydroxide radicals (*OH) [13]. Heterogeneous photocatalysis is used to treat pharmaceutical wastewater thanks to its high efficiency, relatively low cost, chemical stability, and non-toxic compounds production [14]. The photocatalytic removal of MET has been investigated by ZnO, TiO₂, Ga₂O₃,

*Corresponding author. Tel.: +98 313 7934532

E-mail address: m.farhadian@eng.ui.ac.ir

DOI: 10.22104/aet.2020.3952.1196

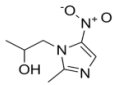
SnO₂/Co₃O₄, CoFe₂O₄, ZnSnO₃, BiVO₄, and Cu₂S/Ag₂S/BiVO₄ [15-18]. TiO₂ is frequently used in photocatalytic processes [19] owing to its non-toxicity, low cost, high photocatalytic activity, and high stability for antibiotics degradation [20,21]. Furthermore, Fe₂O₃ plays an active role in reducing band gap energy and enhancing the photocatalytic activity of TiO₂ [22]. There is an additional increase in the photocatalytic efficiency of TiO₂ using graphite oxide (GO) since it has a positive influence on photocatalytic properties [23]. Previous research shows that hybrid photocatalysts have more photocatalytic activity, resulting in greater removal efficiency [24]. Furthermore, one of the most effective parameters for process efficiency that has attracted the attention of researchers nowadays is the presence of mineral salts such as Na₂SO₄, Fe₂(SO₄)₃, CaCl₂, AlCl₃, FeCl₂, FeCl₃, NaCl, NaHCO₃, Al₂(SO₄)₃, and Na₂CO₃ in solution [25-27]. To the best of our knowledge, no study has investigated the removal of MET from contaminated water with the TiO₂/Fe₂O₃/GO photocatalyst in the presence of mineral salts. The TiO₂/Fe₂O₃/GO photocatalyst, with high efficiency in MET removal, is synthesized through the sol-gel method. This study aims to examine the effects of process factors including MET concentration, photocatalyst concentration, irradiation time, and initial pH on MET removal efficiency via RSM. Under optimal conditions, the effects of mineral salts concentrations, including NaCl, Na₂SO₄, NaHCO₃, KCl, MgSO₄, and CaCl₂, on the removal efficiency of MET are also evaluated.

2. Materials and methods

2.1. Materials

The chemicals employed for the preparation of the photocatalyst are tetra-n-butyl orthotitanate (TBOT), GO, ethanol, HNO₃, and Fe₂O₃.9H₂O; HCl and NaOH were used to adjust the pH of the solution. All of the chemicals in the experiments were purchased from the Merck Co., and the Amin Pharmaceuticals Co., Iran, provided the MET. The properties of the MET are presented in Table 1.

Table 1. MET Specifications

Pharmaceutical name	MET
Trade name	Flagyl
Pharmaceutical type	Antibiotics
Chemical formula	C ₆ H ₉ N ₃ O ₃
Pharmaceutical structure	
Molecular weight (g/mol)	171.15
Water solubility (mg/L)	10500
λ _{max} (nm)	320

2.2. TiO₂/Fe₂O₃/GO synthesis

Based on the screening experiments, the weight ratios of GO/TiO₂ and Fe₂O₃/TiO₂ are chosen to be 0.05 and 0.10, respectively. To synthesize the photocatalyst via the sol-gel method, the GO is first mixed with ethanol, and the solution experiences ultrasound for 1h. Next, the Fe₂O₃.9H₂O and ethanol are mixed in a heater stirrer until the color of the solution becomes orange. Then, TBOT is added to the GO and ethanol solution, and it is mixed until a yellow color is obtained. After adding the Fe₂O₃.9H₂O and ethanol solution as well as the HNO₃ and deionized water to the above solution, the resulting solution is mixed for 1-4 h at 80 °C to form a gel. Finally, the solution is dried in an oven at 80 °C for 24 h, and the calcination process is performed in a muffle furnace at 450 °C for 2 h to obtain the photocatalyst [28]. About 85% of the synthesized photocatalyst have particles whose diameters are below 50 nm.

2.3. Photocatalytic experiments

The removal of MET is performed in a photoreactor with a volume of 100 ml, in which a UV lamp (15 W power and 254 nm wavelength) is devised, and the photoreactor temperature is adjusted at 25±2 °C. A MET solution is prepared for each experiment, and after adjusting its pH, it is transferred to the photoreactor with the desired photocatalyst concentration (see Table 4). The pH of the solution is adjusted by HCl and NaOH using a pHmeter (UB-10-Denver). After the completion of the experiment, the photocatalyst particles of the MET solution are separated by a centrifuge device (HANIL SUPRA 22 K) at 10000 rpm for 20 min. The MET residual concentration is then measured by a spectrophotometer device (V-570, Jasco, Japan) with the MET calibration curve at the maximum wavelength (λ_{max}=320 nm). The efficiency of MET removal is calculated by Equation 1:

$$R = \frac{C_{in} - C_{out}}{C_{in}} \times 100\% \quad (1)$$

where C_{in} and C_{out} (mg/L) are the initial and final MET concentrations.

2.4. Characterization

For the characterization of the synthesized photocatalyst, XRF analysis is performed by an X-ray fluorescence device (S4-Pioneer, Bruker, Germany), and XRD analysis is conducted by an X-ray diffraction device (D-8 Advance, Bruker, Germany). According to the XRD results of the photocatalyst and the Scherrer Equation, the crystallite size of the photocatalysts is determined.

$$\text{Crystallite size (average in } \text{Å}) = \frac{K\lambda}{B \cos\theta} \quad (2)$$

In Equation 2, K is the shape factor (0.9), θ is half of the Bragg angle (in terms of radiant), λ is the wavelength of the used x-ray (1.54 Å), and B is the width of the maximum peak at

half of its height (FWHM). Moreover, FT-IR analysis is performed by a Fourier transform infrared spectrometer FT-IR-6300 (Jasco, Japan), and BET analysis is used to measure the pore volume and surface area of the photocatalyst by means of N₂ adsorption at 77K (Belsorp mini, Japan). UltraViolet-Visible Diffuse Reflection Spectroscopy analysis is also performed by an Ultraviolet-Visible Spectrophotometer (V-670, Jasco, Japan). The band gap energy of the photocatalyst (E) is obtained from the plot of $[F(R) \times E]^{0.5}$ vs. E for indirect band gap semiconductors, in which F(R) is the Kubelka Munk function represented by the following equation [29]:

$$F(R) = \frac{(1 - R)^2}{2R} \quad (3)$$

where R is the reflectance.

3. Results and discussion

3.1. TiO₂/Fe₂O₃/GO Characterization

3.1.1. XRD Analysis

To detect the presence of TiO₂, GO, and Fe₂O₃ nanoparticles, an XRD analysis is conducted. The XRD pattern of the TiO₂/Fe₂O₃/GO photocatalyst is shown in Figure 1. According to the XRD results and using Equation 2, the crystallite size of the synthesized photocatalyst is calculated to be about 4 nm. The photocatalyst has main peaks at 2θ values of 25.3° and 37.8° as well as 27.4° and 35.4°, which are related to the anatase TiO₂ and rutile TiO₂, respectively [30]. Furthermore, Fe³⁺ peaks are observed at 2θ values of 18.2° and 35.2°, and the peak at the 2θ value of 11.09° belongs to GO in the synthesized photocatalyst, corresponding to the reference peaks [31].

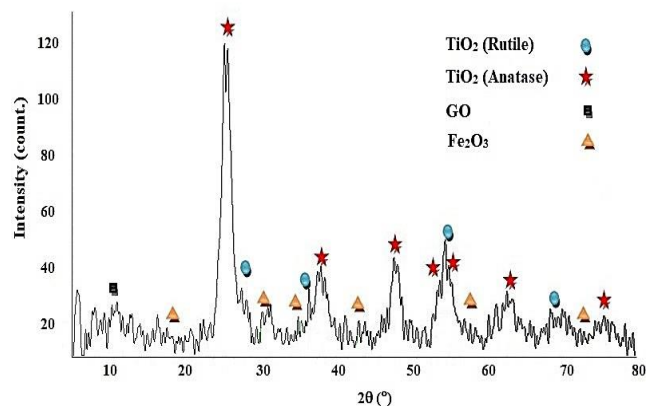


Fig. 1. XRD analysis of TiO₂/Fe₂O₃/GO

3.1.2. XRF Analysis

The XRF analysis is performed on the TiO₂/Fe₂O₃/GO photocatalyst to determine the composition of the different elements in the photocatalyst (Table 2). Based on the results, the synthesized photocatalyst contains 89.39 wt% of TiO₂ and 8.31 wt% of Fe₂O₃, in which the pre-calculated value of the Fe₂O₃/TiO₂ weight ratio 1:10 is obtained successfully. GO is not detectable by XRF due to the low carbon content [32]. The XRD and FT-IR analyses confirm the presence of GO in the photocatalyst.

Table 2. XRF analysis of TiO₂/Fe₂O₃/GO

Compound	TiO ₂ /Fe ₂ O ₃ /GO concentration (wt. %)
TiO ₂	89.39
Fe ₂ O ₃	8.31
SO ₃	0.245
Al ₂ O ₃	0.220
MnO	0.158
Cr ₂ O ₃	0.126
SiO ₂	0.135
CuO	0.051
Cl	0.038
ZnO	0.017
Total	100

3.1.3. FT-IR Analysis

An FT-IR analysis is conducted to determine the functional groups of the TiO₂/Fe₂O₃/GO photocatalyst. According to Figure 2, the peaks observed in the photocatalyst spectrum are related to the superficial hydroxyl group (O-H) of TiO₂ nanoparticles [33], the stretching vibration of the Fe-O functional group of Fe₂O₃ nanoparticles, and the Ti-O-C functional group of TiO₂ nanoparticles [34] at the wave numbers of 3402.78, 534.185, and 1030.77 cm⁻¹, respectively. Moreover, the wave numbers of 1671.98 and 1603.52 cm⁻¹ belong to the C=O functional group [35], and the C-H and C-O functional groups have wave numbers at 1451.17 and 1251.58 cm⁻¹, respectively [36], indicating the presence of GO in the synthesized photocatalyst.

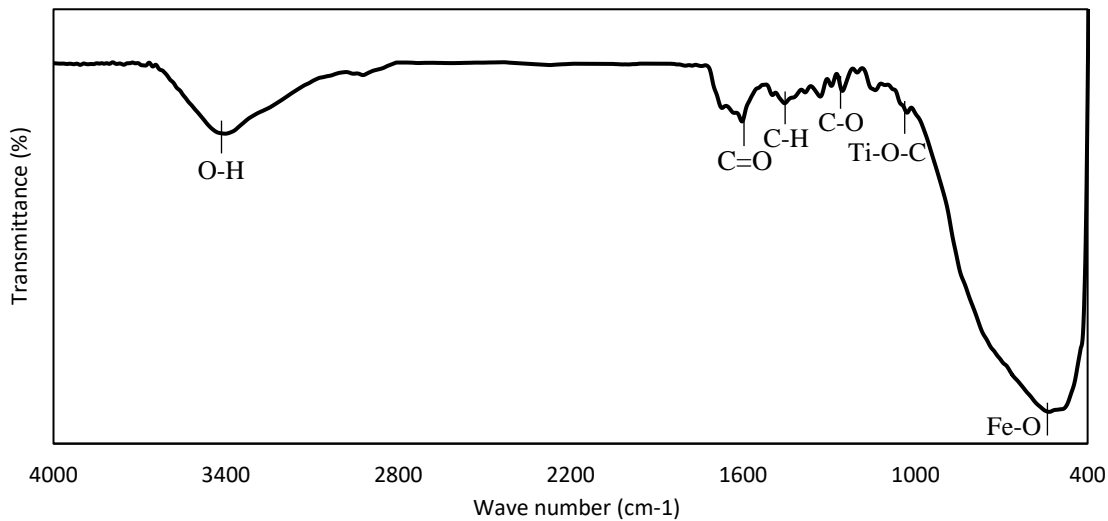


Fig. 2. FT-IR spectrum of TiO₂/Fe₂O₃/GO

3.1.4. UV-Vis DRS Analysis

The UV-Vis DRS spectrum measures the band gap energy of the TiO₂/Fe₂O₃/GO photocatalyst. TiO₂ is an indirect band gap semiconductor [29,37]. As can be seen in Figure 3, the indirect band gap energy of the photocatalyst is obtained as 2.7 eV by Equation 3. The results indicate that the presence of Fe₂O₃ in the structure of the synthesized photocatalyst decreases the band gap energy of TiO₂ (3.4 eV).

3.1.5. BET Analysis

A BET analysis is conducted on the TiO₂/Fe₂O₃/GO photocatalyst to investigate the BET surface area, Langmuir

surface area, pore volume, and average pore diameter. The results are shown in Table 3.

Table 3. BET analysis of TiO₂/Fe₂O₃/GO

Parameter (unit)	Value
BET surface area (m ² /g)	110.73
Langmuir surface area (m ² /g)	147.27
External surface area (m ² /g)	6.613
Micropore surface area (m ² /g)	95.167
Total pore volume (cm ³ /g)	0.1101
Total micropore volume (cm ³ /g)	0.092393
Average pore diameter (nm)	2.6478

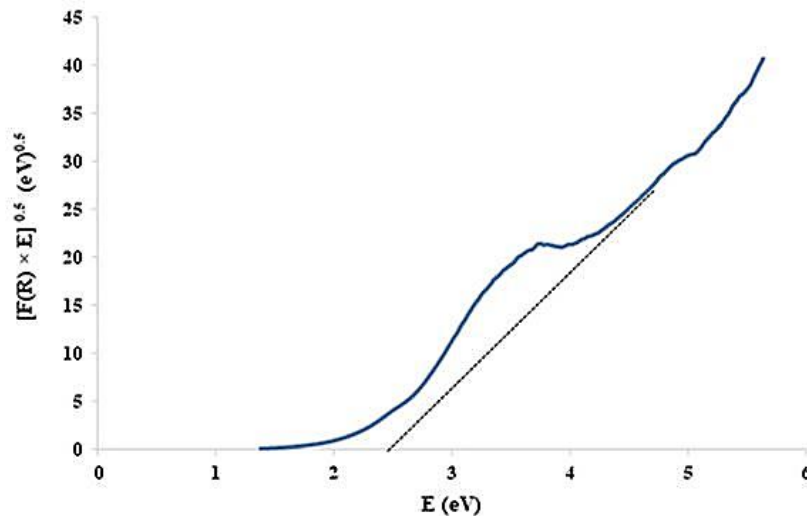


Fig. 3. Band gap determination of TiO₂/Fe₂O₃/GO via Kubelka Munk method

3.2. Results of Photocatalytic Experiments on MET Removal

The central composite design (CCD) is used for design of experiments by RSM to remove the MET with the

TiO₂/Fe₂O₃/GO photocatalyst. For four factors and three levels with six replicates of the central points, 30 runs are conducted to give statistical consistency to the mathematical model. The analysis of the results and the

evaluation of the optimal conditions on MET Removal are determined by the Design Expert software, version 11.0.0. According to Table 4, the effects of the operational factors on MET Removal efficiency are investigated: MET concentration, initial pH, photocatalyst concentration, and irradiation time. Moreover, mineral salts such as NaCl, Na₂SO₄, NaHCO₃, KCl, MgSO₄, and CaCl₂ with concentrations of 50, 100, 200, 400, and 800 mg/L, respectively, are studied under optimal conditions to determine their effect on MET removal efficiency. Other factors, such as temperature (25±2 °C) and UV lamp radiation (15 W power, 254 nm wavelength), are assumed to be constant.

Table 5. ANOVA for MET removal

Model terms	Sum of squares	Degree of freedom	Mean square	P-value	F-value	Status
Model	1009.29	14	97.20	<0.0001	148.40	Significant
A: pH	1.39	1	1.39	0.5625	0.2111	Not significant
B: Irradiation time	5618.06	1	5618.06	<0.0001	854.02	Significant
C: Photocatalyst	98.00	1	98.00	0.0015	14.90	Significant
D: MET concentration	5512.50	1	5512.50	<0.0001	837.98	Significant
A×B	14.06	1	14.06	0.1644	2.14	Not significant
A×C	0.5625	1	0.5625	0.7740	0.0855	Not significant
A×D	0.0625	1	0.0625	0.9236	0.0095	Not significant
B×C	0.5625	1	0.5625	0.7740	0.0855	Not significant
B×D	1040.06	1	1040.06	<0.0001	158.10	Significant
C×D	232.56	1	232.56	<0.0001	35.35	Significant
A ²	232.97	1	232.97	<0.0001	35.41	Significant
B ²	2.68	1	2.68	0.5327	0.4079	Not significant
C ²	372.00	1	372.00	<0.0001	56.55	Significant
D ²	343.69	1	343.69	<0.0001	55.25	Significant
Lack of Fit	2.92	14	2.92	0.9826	0.2099	Not significant

The *P*-value (an index for the significance of factors) and *F*-value (an index for the priority of factors influence) are considered for evaluating the MET removal efficiency. Based on RSM, the factors with a *P*-value less than 0.05 are considered significant (confidence interval 95%). According to Table 5, the presented model is significant (*P*<0.0001), and a non-significant lack of fit indicates that the statistical model is well fitted to the experimental results. Furthermore, the factors of irradiation time, MET concentration, photocatalyst concentration, and pH have the maximum effects on MET removal efficiency. The interactions between the MET concentration and

Table 4. Operational factors and levels

Factors	Levels		
MET concentration (mg/L)	10	15	20
Photocatalyst concentration (g/L)	0.5	1	1.5
Irradiation time (min)	60	90	120
Initial pH	4	5	6

3.2.1. Analysis of variance

The analysis of variance (ANOVA) based on the quadratic model is demonstrated in Table 5.

irradiation time, as well as photocatalyst concentration, play significant roles in the MET removal efficiency. The second-order model, which the Design Expert presents for MET removal, is as Equation 4.

$$R = +51.91 + 24.97 * B + 2.24 * C - 13.47 * D - 12.09 * (B \times D) + 3.81 * (C \times D) - 37.93 * A^2 - 11.98 * C^2 + 11.52 * D^2 \quad (4)$$

The experimental results Figure 4. The *R*² value in the model is 0.98, suggesting a good correspondence between the experimental and the predicted results. Therefore, due

to the proximity of the regression value to unity, RSM is an acceptable method.

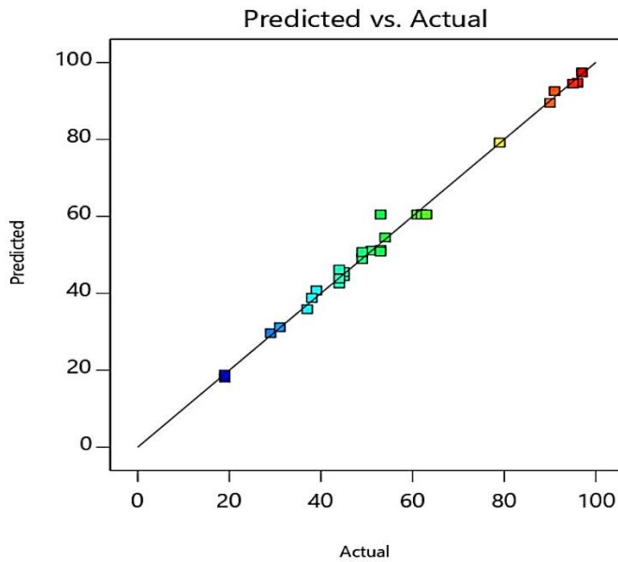


Fig. 4. Experimental results versus predicted results on MET removal efficiency

Pareto analysis is applied to calculate the percentage effect of each factor on the MET removal efficiency by Equation 5 [38].

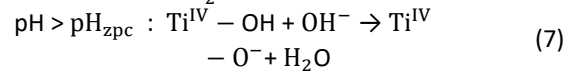
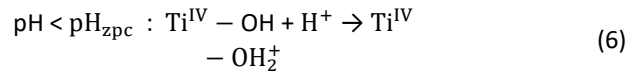
$$P_i = \left(\frac{b_i^2}{\sum b_i^2} \right) \times 100\% \quad (5)$$

where P_i is the percentage effect, and b_i is the coefficient of factor. According to the results, A^2 (53.3%), B (23.1%), D (6.7%), and BD (5.4%) are the most effective factors in MET removal efficiency.

3.2.2. Effects of operational factors

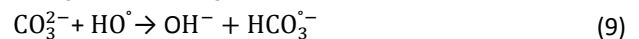
The effects of operational factors on MET removal efficiency are presented in Figure 5. Based on Fig. 5a, the MET removal efficiency increases by 35% with growth in irradiation time from 40 to 100 min at pH=5. Similar results regarding the effect of irradiation time on MET removal efficiency have been reported [10,12]. According to Figure 5b, when the $\text{TiO}_2/\text{Fe}_2\text{O}_3/\text{GO}$ photocatalyst concentration grows from 0.5 to 1.5 g/L at a pH=5, the MET removal efficiency first increases by around 20% and then decreases 15%. As the active sites present on the surface of the photocatalyst and the permeation of UV light towards the photocatalyst increases at low photocatalyst concentrations, it leads to an increase in MET removal efficiency. On the other hand, at high photocatalyst concentrations, the photocatalyst blocks the UV light, and it causes turbidity, decreasing the MET removal efficiency [39]. In a study conducted by Fakhravar *et al.* in 2020, with a growth in the concentration of the catalysts (BiVO_4 and $\text{Cu}_2\text{S}/\text{Ag}_2\text{S}/\text{BiVO}_4$) from 0.5 to 1.5 g/L, the MET removal efficiency first increased and then decreased (MET concentration=50 mg/L, pH=3, $T=25^\circ\text{C}$, and $I=400\text{ W/m}^2$) [18]. According to Figure 5c, at a constant

pH, the MET removal efficiency experiences a 20% drop from 10 to 15 mg/L MET concentration. It occurs because the photocatalyst becomes saturated, which inhibits the generation of pore electron pairs and hydroxyl radicals [40]. The results of this research are in agreement with previous studies [8,15]. In Figure 5, the results of the effect of pH on MET removal efficiency show that the maximum efficiency is achieved at a pH=5. This efficiency for the selected initial pH (4, 5, and 6) has approximately similar results because the pH range is not expanded, and the levels of pH are between the pK_a of the MET (2.94) and pH_{zpc} of the photocatalyst (5.84). In this pH range, MET has positive charges, and the synthesized photocatalyst owns negative charges (see Equations 6 and 7).



3.2.3. Effects of mineral salts

The effects of mineral salts on MET removal efficiency are investigated at pollutant concentration of 20 mg/L, pH=5, $\text{TiO}_2/\text{Fe}_2\text{O}_3/\text{GO}$ photocatalyst concentration: 1 g/L, and irradiation time: 120 min, resulting in removing 65% of the MET. One of the adverse effects of mineral salts on MET removal efficiency is that they influence the pH. As mentioned previously, the optimal pH should be between pK_a and pH_{zpc} . The results demonstrate that NaHCO_3 increases pH, while other mineral salts reduce pH at an optimal initial pH=5 [25]. As seen in Equations 8-11, the presence of HCO_3^- and Cl^- in the MET solution causes the free radicals HO° to consume [41] and to produce radicals that are less reactive, leading to a decrease in MET removal efficiency [36].



Another reason for the decline in MET removal efficiency is that the anions compete with each other to occupy the active sites of the photocatalyst. The presence of mineral salts drops the UV efficiency for generating pore electron pairs. Figure 6 demonstrates the effects of the mineral salts on the reaction rate constant for MET removal efficiency (MET concentration: 20 mg/L, pH=5, photocatalyst concentration: 1 g/L, and irradiation time: 120 min). According to Figure 6, an increase in NaCl and KCl concentrations up to 200 mg/L has a deactivation effect on the reaction rate constant ($K_{\text{NaCl},200}=7.92$ and $K_{\text{KCl},200}=7.48\text{ day}^{-1}$). On the other hand, when the concentrations of NaCl and KCl grow to 800 mg/L, their ionic strength becomes a determinant factor that increases the reaction rate

constant ($K_{NaCl,800}=10.81$ and $K_{KCl,800}=8.92 \text{ day}^{-1}$). In addition, with a growth in mineral salts concentrations up to 800 mg/L, the reaction rate constant decreases for Na_2SO_4

(42.43% deactivation), $MgSO_4$ (38.08%), and $NaHCO_3$ (37.73%), while there is an increase in $CaCl_2$ (12.69%) under the same conditions ($K_{H_2O}=11.5 \text{ day}^{-1}$).

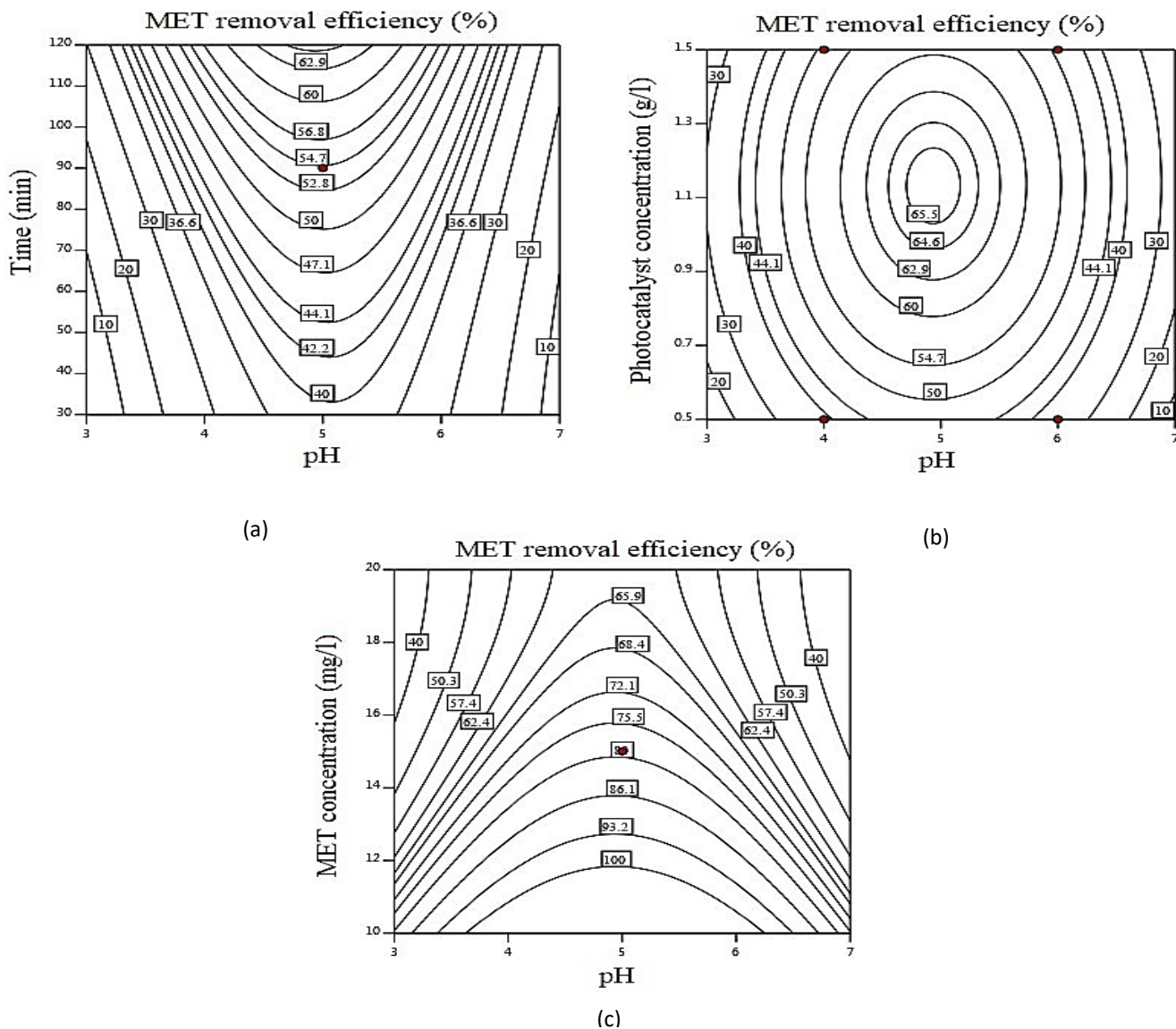


Fig. 5. Counter plots of MET removal efficiency as pH and (a) irradiation time, (b) photocatalyst concentration, and (c) MET concentration

4. Conclusions

The $TiO_2/Fe_2O_3/GO$ photocatalyst has high efficiency for the removal of MET from polluted water. Irradiation time, MET concentration, photocatalyst concentration, and pH have maximum impacts on the MET removal efficiency. Mineral salts lead to a decline in MET removal efficiency since $NaCl$, $MgSO_4$, KCl , Na_2SO_4 , and $CaCl_2$ decrease the pH, and $NaHCO_3$ increases it. The presence of Cl^- and HCO_3^- also produces radicals that are less reactive, leading to a decline in MET removal efficiency. Owing to the ionic strength of

$NaCl$ and KCl in high concentrations, MET removal efficiency first drops and then rises. For future research, these experiments will be conducted in real pharmaceutical wastewater, and the simultaneous presence of the mineral salts and their interactions will be investigated comprehensively.

Acknowledgments

The authors much appreciate the Environmental Research Institute-University of Isfahan for their cooperation and support.

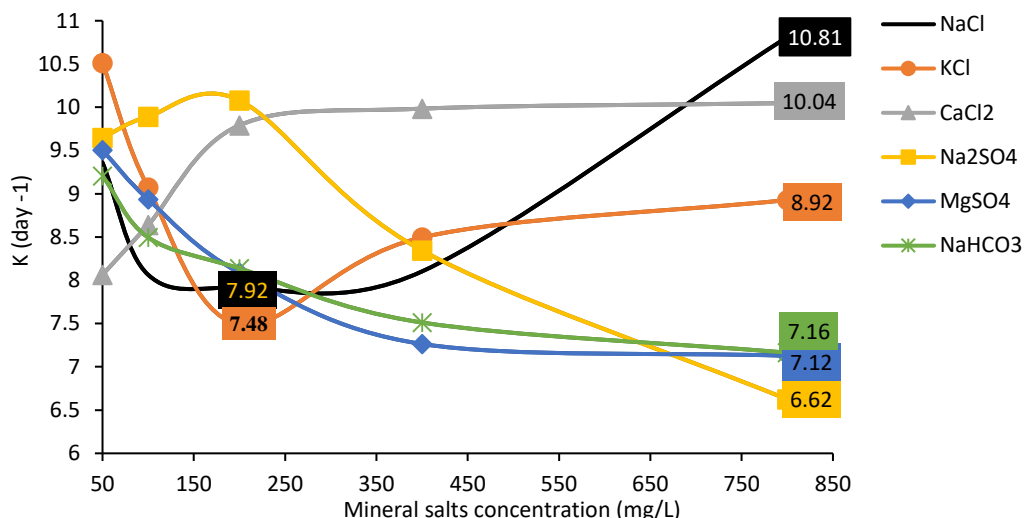


Fig. 6. Effects of mineral salts on reaction rate constant for MET removal efficiency (MET concentration: 20 mg/L, pH=5, photocatalyst concentration: 1 g/L, and irradiation time: 120 min)

References

- [1] amírez-Franco, J.H., Galeano, L.-A., Vicente, M.-A. (2019). Fly ash as photo-Fenton catalyst for the degradation of amoxicillin. *Journal of Environmental chemical engineering*, 7, 103274.
- [2] Hashemi, H., Safari, M., Khodabakhshi, A. (2015). Determination of inhibitory concentration of oxytetracycline on methanogenic bacteria by in vitro study. *Journal of medical bacteriology*, 4, 21-26.
- [3] Amin, M. M., Hashemi, H., Ebrahimi, A., Ebrahimi, A. (2012). Effects of oxytetracycline, tylosin, and amoxicillin antibiotics on specific methanogenic activity of anaerobic biomass. *International journal of environmental health engineering*, 1(1), 37.
- [4] Forouzesh, M., Ebadi, A., Aghaeinejad-Meybodi, A. (2019). Degradation of metronidazole antibiotic in aqueous medium using activated carbon as a persulfate activator. *Separation and purification technology*, 210, 145-151.
- [5] Nasiri, A., Tamaddon, F., Mosslemin, M. H., Gharaghani, M. A., Asadipour, A. (2019). New magnetic nanobiocomposite CoFe₂O₄@ methycellulose: facile synthesis, characterization, and photocatalytic degradation of metronidazole. *Journal of materials science: Materials in eElectronics*, 30(9), 8595-8610.
- [6] Wang, Q., Cai, Z., Huang, L., Pan, Y., Quan, X., Puma, G. L. (2019). Intensified degradation and mineralization of antibiotic metronidazole in photo-assisted microbial fuel cells with Mo-W catalytic cathodes under anaerobic or aerobic conditions in the presence of Fe (III). *Chemical engineering journal*, 376, 119566.
- [7] Malakootian, M., Olama, N., Malakootian, M., Nasiri, A. (2019). Photocatalytic degradation of metronidazole from aquatic solution by TiO₂-doped Fe³⁺ nanophotocatalyst. *International journal of environmental science and technology*, 16, 4275-4284.
- [8] Wang, X., Wang, A., Lu, M., Ma, J. (2018). Synthesis of magnetically recoverable Fe⁰/graphene-TiO₂ nanowires composite for both reduction and photocatalytic oxidation of metronidazole. *Chemical engineering journal*, 337, 372-384.
- [9] Neghi, N., Krishnan, N.R., Kumar, M. (2018). Analysis of metronidazole removal and micro-toxicity in photolytic systems: Effects of persulfate dosage, anions and reactor operation-mode. *Journal of environmental chemical engineering*, 6, 754-761.
- [10] Xu, L., Yang, Y., Li, W., Tao, Y., Sui, Z., Song, S., Yang J. (2019). Three-dimensional macroporous graphene-wrapped zero-valent copper nanoparticles as efficient micro-electrolysis-promoted Fenton-like catalysts for metronidazole removal. *Science of the total environment*, 658, 219-233.
- [11] Cuerda-Correa, E. M., Alexandre-Franco, M. F., Fernández-González, C. (2020). Advanced oxidation processes for the removal of antibiotics from water. An overview. *ater*, 12(1), 102.
- [12] Feng, J., Sun, J., Liu, X., Zhu, J., Tian, S., Wu, R., Xiong, Y. (2020). Coupling effect of piezomaterial and DSA catalyst for degradation of metronidazole: Finding of induction electrocatalysis from remnant piezoelectric filed. *Journal of catalysis*, 381, 530-539.
- [13] Changotra, R., Rajput, H., Dhir, A. (2019). Treatment of real pharmaceutical wastewater using combined approach of Fenton applications and aerobic biological treatment. *Journal of photochemistry and photobiology A: Chemistry*, 376, 175-184
- [14] Davari, N., Farhadian, M., Solaimany Nazar, A.R., Homayoonfal, M. (2017). Degradation of diphenhydramine by the photocatalysts of ZnO/Fe₂O₃ and TiO₂/Fe₂O₃ based on clinoptilolite: Structural and operational comparison. *Journal of environmental chemical engineering*, 5, 5707-5720.

- [15] Davari, N., Farhadian, M., Solaimany Nazar, A.R. (2019). Synthesis and characterization of Fe₂O₃ doped ZnO supported on clinoptilolite for photocatalytic degradation of metronidazole. *Environmental technology*, 1-13.
- [16] Cai-Yun, L., Zheng-Feng, Y., Paul, B. (2020). Facile synthesis of spinel CoFe₂O₄ nanoparticle and its application as magnetic recoverable photocatalyst for degradation of metronidazole and some selected organic dyes. *Journal of nanoscience and nanotechnology*, 20, 1209-1214.
- [17] Dong, S., Cui, L., Zhang, W., Xia, L., Zhou, S., Russell, C.K., Fan, M., Feng, J., Sun, J. (2020). Double-shelled ZnSnO₃ hollow cubes for efficient photocatalytic degradation of antibiotic wastewater. *Chemical engineering journal*, 384, 123279.
- [18] Fakhrafar, S., Farhadian, M., Tangestaninejad, S. (2020). Excellent performance of a novel dual Z-scheme Cu₂S/Ag₂S/BiVO₄ heterostructure in metronidazole degradation in batch and continuous systems: Immobilization of catalytic particles on α -Al₂O₃ fiber. *Applied surface science*, 505, 144599.
- [19] Darvishi Cheshmeh Soltani R., Rezaee A., Rezaee R., Safari M., Hashemi H. (2015). Photocatalytic degradation of methylene blue dye over immobilized ZnO nanoparticles: Optimization of calcination conditions, *Journal of advances in environmental health research*, 3, 8-14.
- [20] Magnone, E., Kim, M.-K., Lee, H.J., Park, J.H. (2019). Testing and substantial improvement of TiO₂/UV photocatalysts in the degradation of Methylene blue. *Ceramics international*, 45, 3359-3367.
- [21] Moeini, Z., Azhdarpoor, A., Yousefinejad, S., Hashemi, H. (2019). Removal of atrazine from water using titanium dioxide encapsulated in salicylaldehyde-NH₂-MIL-101 (Cr): Adsorption or oxidation mechanism. *Journal of cleaner production*, 224, 238-245.
- [22] Sharma, B., Boruah, P.K., Yadav, A., Das, M.R. (2018). TiO₂-Fe₂O₃ nanocomposite heterojunction for superior charge separation and the photocatalytic inactivation of pathogenic bacteria in water under direct sunlight irradiation. *Journal of environmental chemical engineering*, 6, 134-145.
- [23] Naraginti S., Yong Y.C. (2019). Enhanced detoxification of p-bromophenol by novel Zr/Ag-TiO₂@rGO ternary composite: Degradation kinetics and phytotoxicity evolution studies. *Ecotoxicology and environmental safety*, 170, 355-362.
- [24] Siwińska-Stefańska, K., Fluder, M., Tylus, W., Jesionowski T. (2018). Investigation of amino-grafted TiO₂/reduced graphene oxide hybrids as a novel photocatalyst used for decomposition of selected organic dyes. *Journal of environmental management*, 212, 395-404.
- [25] Rioja, N., Zorita, S., Peñas, F.J. (2016). Effect of water matrix on photocatalytic degradation and general kinetic modeling. *Applied catalysis B: Environmental*, 180, 330-335.
- [26] Chen, P., Zhang, Q., Shen, L., Tan, R. Li, Chen, C., T., Liu, H., Liu, Y., Cai, Z., Liu, G., Lv, W. (2019). Insights into the synergetic mechanism of a combined vis-RGO/TiO₂/peroxodisulfate system for the degradation of PPCPs: Kinetics, environmental factors and products. *Chemosphere*, 216, 341-351.
- [27] Wu, Y., Fang, Z., Shi, Y., Chen, H., Liu, Y., Wang, Y., Dong, W. (2019). Activation of peroxy monosulfate by BiOCl@Fe₃O₄ catalyst for the degradation of atenolol: Kinetics, parameters, products and mechanism. *Chemosphere*, 216, 248-257.
- [8] Wang, X., Wang, A., Lu, M., Ma, J. (2018). Synthesis of magnetically recoverable Fe⁰/graphene-TiO₂ nanowires composite for both reduction and photocatalytic oxidation of metronidazole. *Chemical engineering journal*, 337, 372-384.
- [9] Neghi, N., Krishnan, N.R., Kumar, M. (2018). Analysis of metronidazole removal and micro-toxicity in photolytic systems: Effects of persulfate dosage, anions and reactor operation-mode. *Journal of environmental chemical engineering*, 6, 754-761.
- [10] Xu, L., Yang, Y., Li, W., Tao, Y., Sui, Z., Song, S., Yang J. (2019). Three-dimensional macroporous graphene-wrapped zero-valent copper nanoparticles as efficient micro-electrolysis-promoted Fenton-like catalysts for metronidazole removal. *Science of the total environment*, 658, 219-233.
- [11] Cuerda-Correa, E. M., Alexandre-Franco, M. F., Fernández-González, C. (2020). Advanced oxidation processes for the removal of antibiotics from water. An overview. *ater*, 12(1), 102.
- [12] Feng, J., Sun, J., Liu, X., Zhu, J., Tian, S., Wu, R., Xiong, Y. (2020). Coupling effect of piezomaterial and DSA catalyst for degradation of metronidazole: Finding of induction electrocatalysis from remnant piezoelectric filed. *Journal of catalysis*, 381, 530-539.
- [13] Changotra, R., Rajput, H., Dhir, A. (2019). Treatment of real pharmaceutical wastewater using combined approach of Fenton applications and aerobic biological treatment. *Journal of photochemistry and photobiology A: Chemistry*, 376, 175-184
- [14] Davari, N., Farhadian, M., Solaimany Nazar, A.R., Homayoonfal, M. (2017). Degradation of diphenhydramine by the photocatalysts of ZnO/Fe₂O₃ and TiO₂/Fe₂O₃ based on clinoptilolite: Structural and operational comparison. *Journal of environmental chemical engineering*, 5, 5707-5720.
- [15] Davari, N., Farhadian, M., Solaimany Nazar, A.R. (2019). Synthesis and characterization of Fe₂O₃ doped ZnO supported on clinoptilolite for photocatalytic

- degradation of metronidazole. *Environmental technology*, 1-13.
- [16] Cai-Yun, L., Zheng-Feng, Y., Paul, B. (2020). Facile synthesis of spinel CoFe_2O_4 nanoparticle and its application as magnetic recoverable photocatalyst for degradation of metronidazole and some selected organic dyes. *Journal of nanoscience and nanotechnology*, 20, 1209-1214.
- [17] Dong, S., Cui, L., Zhang, W., Xia, L., Zhou, S., Russell, C.K., Fan, M., Feng, J., Sun, J. (2020). Double-shelled ZnSnO_3 hollow cubes for efficient photocatalytic degradation of antibiotic wastewater. *Chemical engineering journal*, 384, 123279.
- [18] Fakhravar, S., Farhadian, M., Tangestaninejad, S. (2020). Excellent performance of a novel dual Z-scheme $\text{Cu}_2\text{S}/\text{Ag}_2\text{S}/\text{BiVO}_4$ heterostructure in metronidazole degradation in batch and continuous systems: Immobilization of catalytic particles on $\alpha\text{-Al}_2\text{O}_3$ fiber. *Applied surface science*, 505, 144599.
- [19] Darvishi Cheshmeh Soltani R., Rezaee A., Rezaee R., Safari M., Hashemi H. (2015). Photocatalytic degradation of methylene blue dye over immobilized ZnO nanoparticles: Optimization of calcination conditions, *Journal of advances in environmental health research*, 3, 8-14.
- [20] Magnone, E., Kim, M.-K., Lee, H.J., Park, J.H. (2019). Testing and substantial improvement of TiO_2/UV photocatalysts in the degradation of Methylene blue. *Ceramics international*, 45, 3359-3367.
- [21] Moeini, Z., Azhdarpoor, A., Yousefinejad, S., Hashemi, H. (2019). Removal of atrazine from water using titanium dioxide encapsulated in salicylaldehyde- NH_2 -MIL-101 (Cr): Adsorption or oxidation mechanism. *Journal of cleaner production*, 224, 238-245.
- [22] Sharma, B., Boruah, P.K., Yadav, A., Das, M.R. (2018). $\text{TiO}_2\text{-Fe}_2\text{O}_3$ nanocomposite heterojunction for superior charge separation and the photocatalytic inactivation of pathogenic bacteria in water under direct sunlight irradiation. *Journal of environmental chemical engineering*, 6, 134-145.
- [23] Naraginti S., Yong Y.C. (2019). Enhanced detoxification of p-bromophenol by novel $\text{Zr}/\text{Ag-TiO}_2/\text{rGO}$ ternary composite: Degradation kinetics and phytotoxicity evolution studies. *Ecotoxicology and environmental safety*, 170, 355-362.
- [24] Siwińska-Stefańska, K., Fluder, M., Tylus, W., Jesionowski T. (2018). Investigation of amino-grafted $\text{TiO}_2/\text{reduced graphene oxide}$ hybrids as a novel photocatalyst used for decomposition of selected organic dyes. *Journal of environmental management*, 212, 395-404.
- [25] Rioja, N., Zorita, S., Peñas, F.J. (2016). Effect of water matrix on photocatalytic degradation and general kinetic modeling. *Applied catalysis B: Environmental*, 180, 330-335.
- [26] Chen, P., Zhang, Q., Shen, L., Tan, R. Li, Chen, C., T., Liu, H., Liu, Y., Cai, Z., Liu, G., Lv, W. (2019). Insights into the synergetic mechanism of a combined vis-RGO/ TiO_2 /peroxodisulfate system for the degradation of PPCPs: Kinetics, environmental factors and products. *Chemosphere*, 216, 341-351.
- [27] Wu, Y., Fang, Z., Shi, Y., Chen, H., Liu, Y., Wang, Y., Dong, W. (2019). Activation of peroxy monosulfate by $\text{BiOCl}/\text{Fe}_3\text{O}_4$ catalyst for the degradation of atenolol: Kinetics, parameters, products and mechanism. *Chemosphere*, 216, 248-257.
- [28] Prabhakar Rao, N., Chandra, M.R., Rao T.S. (2017). Synthesis of Zr doped $\text{TiO}_2/\text{reduced Graphene Oxide}$ (rGO) nanocomposite material for efficient photocatalytic degradation of Eosin Blue dye under visible light irradiation. *Journal of alloys and compounds*, 694, 596-606.
- [29] Goodall, J. B., Kellici, S., Illsley, D., Lines, R., Knowles, J. C., Darr, J. A. (2014). Optical and photocatalytic behaviours of nanoparticles in the Ti-Zn-O binary system. *Rsc Advances*, 4(60), 31799-31809.
- [30] Jokar Baloochi, S., Solaimany Nazar, A.R., Farhadian, M. (2018). 2,4-Dichlorophenoxyacetic acid herbicide photocatalytic degradation by zero-valent iron / titanium dioxide based on activated carbon. *Environmental nanotechnology, monitoring and management*, 10, 212-222.
- [31] Jo, W.-K., Selvam, N.C.S. (2015). Synthesis of GO supported $\text{Fe}_2\text{O}_3\text{-TiO}_2$ nanocomposites for enhanced visible-light photocatalytic applications. *Dalton transactions*, 44, 16024-16035.
- [32] Qiu, Y., Wang, X., Huang, H., Cheng, Z., Chang, X., Guo L. (2019). Ferrocenyl-functionalized carbon nanotubes with greatly improved surface reactivity for enhancing electrocapacitance. *Journal of organometallic chemistry*, 880, 349-354.
- [33] Kannaiyan, D., Kochuveedu, S.T., Jang, Y.H., Jang, Y.J., Lee, J.Y., Lee, J., Lee, J., Kim, J., Kim, D.H. (2010). Enhanced photophysical properties of nanopatterned Titania nanodots/nanowires upon hybridization with Silica via block copolymer templated sol-gel process. *Polymers*, 2, 490-504.
- [34] Taghvaei H., Farhadian M., Davari N., Maazi S. (2017). Preparation, characterization and photocatalytic degradation of methylene blue by Fe^{3+} doped TiO_2 supported on natural zeolite using response surface methodology. *Advances in environmental technology*, 3, 205-216.
- [35] Qu, S., Xiong, Y., Zhang, J. (2019). Fabrication of GO/CDots/ BiOI nanocomposites with enhanced photocatalytic 4-chlorophenol degradation and mechanism insight. *Separation and purification technology*, 210, 382-389.
- [36] Wu, Y., Li, C., Meng, M., Lv, P., Liu, X., Yan, Y. (2019). Fabrication and evaluation of GO/ TiO_2 -based

- molecularly imprinted nanocomposite membranes by developing a reformative filtering strategy: Application to selective adsorption and separation membrane. *Separation and purification technology*, 212, 245-254.
- [37] Tunc, I., Bruns, M., Gliemann, H., Grunze, M., Koelsch, P. (2010). Bandgap determination and charge separation in Ag@TiO₂ core shell nanoparticle films. *Surface and interface analysis*, 42, 835-841.
- [38] Hosseini, S.A., Davodian, M., Abbasian, A.R. (2017). Remediation of phenol and phenolic derivatives by catalytic wet peroxide oxidation over Co-Ni layered double nano hydroxides. *Journal of the Taiwan institute of chemical engineers*, 75, 97-104.
- [39] Rajoriya, S., Bargole, S., George, S., Saharan, V.K., Gogate, P.R., Pandit, A.B. (2019). Synthesis and characterization of samarium and nitrogen doped TiO₂ photocatalysts for photo-degradation of 4-acetamidophenol in combination with hydrodynamic and acoustic cavitation. *Separation and purification technology*, 209, 254-269.
- [40] Dai, Q., Zhou, J., Weng, M., Luo, X., Feng, D., Chen, J. (2016). Electrochemical oxidation metronidazole with Co modified PbO₂ electrode: Degradation and mechanism. *Separation and purification technology*, 166, 109-116.
- [41] Zhang, L., Ma, H., Huang, X., Yan, Z., Ding, W., Li, Z., Cang, D. (2019). Fast and efficient inactivation of antibiotic resistant Escherichia coli by iron electrode-activated sodium peroxydisulfate in a galvanic cell. *Chemical engineering journal*, 355, 150-158.